

Numerical linear stability analysis of round galactic disks

C. Pichon^{1,2}, & R. C. Cannon^{3,4}

1 Astronomisches Institut Universität Basel, Venusstrasse 7
CH-4102 Binningen Switzerland

2 CITA, McLennan Labs, University of Toronto,
60 St. George Street, Toronto, Ontario M5S 1A7.

3 Observatoire de Lyon, 9 Avenue Charles André
69 561 Saint Genis Laval, France.

4 University of Southampton, Bassett Crescent East
Southampton SO16 7PX, United Kingdom.

ABSTRACT

The method originally developed by Kalnajs for the numerical linear stability analysis of round galactic disks is implemented in the regimes of non-analytic transformations between position space and angle-action space, and of vanishing growth rates. This allows effectively any physically plausible disk to be studied, rather than only those having analytic transformations into angle-action space which have formed the primary focus of attention to date. The transformations are constructed numerically using orbit integrations in real space, and the projections of orbit radial actions on a given potential density basis are Fourier transformed to obtain a dispersion relation in matrix form. Nyquist diagrams are used to isolate modes growing faster than a given fraction of the typical orbital period and to assess how much extra mass would be required to reduce the growth rate of the fastest mode below this value. To verify the implementation, the fastest $m = 2$ growth rates of the isochrone and the Kuzmin-Toomre disks are recovered, and the weaker $m = 2$ modes are computed. The evolution of those growth rates as a function of the halo mass is also calculated, and some $m = 1$ modes are derived as illustration. Algorithmic constraints on the method's scope are assessed and its application to observed disks is discussed.

keywords: Galaxies – methods: analytical, numerical – stability, dynamics, disks – bars.

To appear in *Monthly Notices of the Royal Astronomical Society*

1. Introduction

Theoretical studies of the stability of thin stellar disks provide useful constraints on models of galactic formation and dynamics. Disk models can be excluded as unrealistic if they are found to be very unstable and the results of galaxy formation studies can be clarified where they lead to models close to marginal stability. When applied to observed disks, stability analysis provides a unique tool to probe what fraction of the mass is in luminous form via the requirement that there be enough extra matter to make the observed distribution stable over a period comparable to the age of the galaxy.

Three main approaches have been adopted for disk stability analysis: direct N-body simulations, N-body simulations where the bodies are smeared onto a biorthonormal basis thereby solving Poisson's equation implicitly, and linear modal analysis. The first has been widely used, initially by Hohl (1971)⁹, and more recently, *e.g.* by Athanasoula & Sellwood (1985)¹. It provides a flexible tool of investigation which can be carried into the non-linear regime. These simulations, however, only provide insight into instabilities in

the statistical sense, and generally probe poorly the marginal stability regime. This drawback has recently been addressed by Earn & Sellwood (1995)⁷ who developed the second approach of solving Poisson’s equation through a biorthonormal basis. The stability of stellar systems has also been explored for spherical systems via a global “energy principle” (see Sygnet & Kandrup. (1984)²⁵) but this approach has not been successfully implemented for disks because of resonances (Lynden-Bell & Ostriker (1967)¹⁷). Moreover, the method usually provides stability statements which are of little practical use, since no time scale for the astrophysically relevant growth rates is available.

The third method, linear modal analysis (Kalnajs (1977)¹⁴, Zang (1979)²⁷ Hunter (1992)¹¹), is used here. In spite of the obvious limitation to perturbations of small amplitudes it has several potential advantages. In this approach the integro-differential equation resulting from self-consistent solutions of the Boltzmann and Poisson equations is recast into a non-linear eigen-problem using an appropriately defined orthonormal basis. The method, pioneered by Kalnajs (1971-77)^{12,13,14} on the linear stability of galactic disks, involves the formulation of the dynamical perturbed equations in angle-action coordinates and the restriction to a (finite) set of perturbed densities which diagonalise Poisson’s equation in position space. Kalnajs’ original work¹² concerned the stability of the isochrone disk for which explicit transformations between angle-action and position-velocity coordinates exist. Zang (1979)²⁷ studied the self-similar Mestel disks in the same way. More recently, the method was implemented by Hunter (1992)¹¹ (via repeated evaluation of elliptical integrals) for the infinite Kuzmin-Toomre disk. The approach of these authors involved calculating explicit transformations between angle-action variables and position-velocity variables and was therefore restricted to a very limited set of simple analytic disks. More recently, the relevant angle action integrals were computed by quadrature by Weinberg (1991)²⁸, and Bertin (1994)³ while studying the stability of spherical systems for which the Hamiltonian is separable. Finally Vauterin and Dejonghe (1996)²⁶ carried out a similar analysis for disks while performing the whole investigation in position space.

Here, the first step of mapping the distribution function into angle-action space is implemented numerically by calculating the appropriate transformations from the results of integrating unperturbed orbits in the mean field of the galaxy. This then allows considerable freedom in the initial equilibrium to be studied, including the prospect of applying linear stability analysis to distribution functions recovered for observed galaxies. This method is not restricted to integrable potentials and could be generalised to 3D. It can in particular be implemented for *measured* distribution functions, where the potential is deduced from the rotation curve.

In section 2 Kalnajs’ matrix method is recovered following an indirect route corresponding to a rewriting of Boltzmann’s and Poisson’s equations directly in action space. The stability criteria are then reformulated in a form suitable for numerical evaluation of the matrix elements in Section 3. Details of the numerical method are presented and its range of validity is discussed. Section 4 contains results of calculations for the isochrone and the Kuzmin-Toomre disks. These are in agreement with those found by Kalnajs (1978)¹⁵, Earn & Sellwood (1995)⁷, Athanassoula & Sellwood (1985)¹ and Hunter (1992)¹¹. Prospects and applications to observed data as probes of dark matter are sketched in the last section.

2. Linear stability analysis revisited

Linear stability analysis concerns the dynamical evolution of initially small perturbations in their own self-consistent field. The derivation (see *eg* Kalnajs (1977)¹⁴, Sellwood & Wilkinson (1993)²⁴) of the resulting integro-differential equation is sketched here putting the emphasis on a coherent description in action space. This analysis is to be contrasted with that of Vauterin & Dejonghe (1996)²⁶ who chose to implement stability analysis for disks in position space alone. The resulting dispersion relation, Eq. (2.17), is fully equivalent to Kalnajs’ Eq. K-15, but the intermediate integral equation, Eq. (2.11), also provides a connection with orbital stability analysis (Lynden-Bell (1979)¹⁸, Pichon & Lynden-Bell (1992)²⁰ and Collett (1995)⁴).

2.1. The integral equation

The Boltzmann-Vlasov equation,

$$\partial F / \partial t + [H, F] = 0, \quad (2.1)$$

governs the dynamical evolution of an ensemble of collisionless stars. Here H is the Hamiltonian for the motion of one star, F is the mass-weighted distribution function in phase space, and the square bracket denotes the Poisson bracket. Writing $F = F_0 + f$, and $\Psi = \psi_0 + \psi$, where F_0, ψ_0 are the unperturbed distribution function and potential respectively, and linearising Eq. (2.1) in f and ψ , the perturbed distribution function and potential, yields

$$\partial f / \partial t + [H_0, f] - [\psi, F_0] = 0. \quad (2.2)$$

According to Jeans' theorem, the unperturbed equation, $[H_0, F_0] = 0$, is solved if F_0 is any function only of the specific energy, ε , and the specific angular momentum, h .

Following Lynden-Bell and Kalnajs (1972)⁵, angle and action variables of the unperturbed Hamiltonian H_0 are chosen here as canonical coordinates in phase-space. The unperturbed Hamilton equations are quite trivial in these variables, which makes them suitable for perturbation theory in order to study quasi-resonant orbits. The actions are defined in terms of the polar coordinates, (R, θ) , by $\mathbf{J} = (J_R, J_\theta)$, where

$$J_R = (2\pi)^{-1} \oint [\dot{R}] dR, \quad \text{and} \quad J_\theta = h = R^2 \dot{\theta}. \quad (2.3)$$

Here $[\dot{R}]$ is a function of the radius, R , the specific energy, ε , and the specific angular momentum, h , given by $[\dot{R}] = \sqrt{2\varepsilon + 2\psi_0(R) - h^2/R^2}$. The angle between apocentres is $\Theta = \oint h/R^2 [\dot{R}]^{-1} dR$. For a radial period T_R , and a pair of azimuthal and radial epicyclic frequencies Ω , and κ , given by $\Omega = \Theta/T_R$ and $\kappa = 2\pi/T_R$ the phase-angles conjugate to J_R and h are $\varphi = (\varphi_R, \varphi_\theta)$, where

$$\varphi_R = \kappa \int^R [\dot{R}]^{-1} dR, \quad \text{and} \quad \varphi_\theta = \theta + \int^R (h/R^2 - \Omega) [\dot{R}]^{-1} dR. \quad (2.4)$$

The stationary unperturbed Boltzmann equation Eq. (2.1) is solved by any distribution function of the form $F = F_0(\mathbf{J})$, since $[H_0, \mathbf{J}] = 0$.

For growing instabilities, f and ψ are both taken to be proportional to $e^{-i\omega t}$, ω having a positive imaginary part. When expanded in Fourier series with respect to the angles φ , Eq. (2.2) becomes after simple algebra (Kalnajs 1977¹⁴)

$$f_{\mathbf{m}} = \frac{m^{-1} \mathbf{m} \cdot \partial F_0 / \partial \mathbf{J}}{\Omega_\ell - \Omega_p} \psi_{\mathbf{m}}, \quad (2.5)$$

where \mathbf{m} is a integer vector with components (ℓ, m) , $\Omega_\ell = m^{-1} \mathbf{m} \cdot \boldsymbol{\Omega} = \Omega + \ell\kappa/m$, $\boldsymbol{\Omega}$ stands for (κ, Ω) , and $\Omega_p = \omega/m$. Here $\psi_{\mathbf{m}}$ and $f_{\mathbf{m}}$ are the Fourier transforms of ψ and f with respect to $(\varphi_R, \varphi_\theta)$; for instance

$$\psi_{\mathbf{m}}(\mathbf{J}) = \frac{1}{4\pi^2} \int \psi(R, \theta) \exp[-i(\mathbf{m} \cdot \varphi)] d^2\varphi. \quad (2.6)$$

Poisson's integral relates the potential, ψ , to the density perturbation:

$$\psi(R', \theta') = 4\pi G \int \frac{f(\mathbf{R}, \mathbf{v})}{|\mathbf{R} - \mathbf{R}'|} dR d\theta dv_R dv_\theta. \quad (2.7)$$

This equation may be rewritten in order to make explicit the contribution from the interaction of orbits. Here again angle-action variables are useful, as a given unperturbed orbit is entirely specified by its actions. It is therefore straightforward to identify in Poisson's integral the contribution corresponding to the interaction of given orbits. Re-expressing this equation in terms of angles and actions (φ, \mathbf{J}) , using Parseval's theorem and taking its Fourier transform with respect to φ leads to:

$$\psi_{\mathbf{m}}(\mathbf{J}) = 4\pi G \sum_{\mathbf{m}'} \int f_{\mathbf{m}'}(\mathbf{J}') A_{\mathbf{m}\mathbf{m}'}(\mathbf{J}, \mathbf{J}') d^2J', \quad (2.8)$$

where $\psi_{\mathbf{m}}$ and $f_{\mathbf{m}}$ are given by Eq. (2.6) and

$$A_{\mathbf{m}\mathbf{m}'} = \frac{1}{(2\pi)^4} \int \frac{\exp i(\mathbf{m}' \cdot \boldsymbol{\varphi}' - \mathbf{m} \cdot \boldsymbol{\varphi})}{|\mathbf{R} - \mathbf{R}'|} d^2\boldsymbol{\varphi}' d^2\boldsymbol{\varphi}. \quad (2.9)$$

The double sum in Eq. (2.8) extends in both ℓ and m from minus infinity to infinity where the radii $\mathbf{R}(\boldsymbol{\varphi}, \mathbf{J})$ and $\mathbf{R}(\boldsymbol{\varphi}', \mathbf{J}')$ are re-expressed as functions of these variables. Now $|\mathbf{R} - \mathbf{R}'|$ depends on φ_θ and φ'_θ in the combination $\varphi'_\theta - \varphi_\theta \equiv \Delta\varphi$ only. As $|\partial(\varphi'_\theta \varphi_\theta) / \partial(\Delta\varphi \varphi_\theta)| = 1$, the order of integration in Eq. (2.9) may then be reversed, doing the φ_θ integration with $\Delta\varphi$ fixed. This yields $2\pi\delta_{mm'}$, so \mathbf{m}' becomes (ℓ', m) in the surviving terms. This gives for Eq. (2.9)

$$A_{\mathbf{m}\mathbf{m}'} = \frac{2\pi\delta_{mm'}}{(2\pi)^4} \int \frac{\exp i(m\Delta\varphi - \ell'\varphi'_R + \ell\varphi_R)}{|\mathbf{R} - \mathbf{R}'|} d\Delta\varphi d\varphi'_R d\varphi_R. \quad (2.10)$$

Each m mode therefore evolves independently. The dependence on m will be implicit from now on. So, for example, ψ_ℓ is the Fourier transform of $\psi(R, \theta)$ with respect to both φ_R and φ_θ .

Putting Eq. (2.5) into Eq. (2.8) leads to the integral equation

$$\psi_{\ell_1}(\mathbf{J}_1) = 4\pi G \sum_{\ell_2} \int A_{\ell_1\ell_2}(\mathbf{J}_1, \mathbf{J}_2) \frac{m_2^{-1} \mathbf{m}_2 \cdot \partial F_0 / \partial \mathbf{J}_2}{\Omega_{\ell_2} - \Omega_p} \psi_{\ell_2}(\mathbf{J}_2) d^2\mathbf{J}_2. \quad (2.11)$$

This equation is the integral equation for the linear growing mode with an m -fold symmetry of a thin disk. Eq. (2.11) was later approximated by Pichon & Lynden-Bell (1992)²⁰ Collett (1995)⁴ Lynden-Bell (1995) to analyse the growth of the perturbation in terms of a Landau instability.

2.2. The dispersion relation

The perturbed distribution function and potential are now expanded over a potential-distribution basis $\{f^{(n)}\}_n, \{\psi^{(n)}\}_n$ as

$$f(R, V) = \sum_n a_n f^{(n)}(R, V), \quad \text{and} \quad \psi(R) = \sum_n a_n \psi^{(n)}(R), \quad (2.12)$$

where the basis is assumed to satisfy Poisson's equation Eq. (2.7), which when written in action space has Fourier components obeying (following Eq. (2.8) and given Eq. (2.10)):

$$\psi_\ell^{(n)}(\mathbf{J}) = 4\pi G \sum_{\ell'} \int f_{\ell'}^{(n)}(\mathbf{J}') A_{\ell\ell'}(\mathbf{J}, \mathbf{J}') d^2\mathbf{J}'. \quad (2.13)$$

For basis functions scaling like $\exp(im'\theta)$ (preserving the axial symmetry described above), Eq. (2.6) applied to, say, $\psi^{(n)}(R) \exp(im'\theta)$ gives for the Fourier mode ℓ :

$$\psi_\ell^{(n)}(\mathbf{J}) = \frac{1}{2\pi} \int_0^{2\pi} e^{-i\ell\varphi_R} \psi^{(n)}(R[\varphi_R]) e^{im\delta\theta(\varphi_R)} d\varphi_R, \quad (2.14)$$

where Eq. (2.4) has been used to define the relative azimuthal increment $\delta\theta(\varphi_R) \equiv \varphi_\theta - \theta$.

Expanding ψ over this basis (using the *same* expansion for all ℓ s) according to Eq. (2.12), inserting this expansion into Eq. (2.11), multiplying by $f_\ell^{(p)*}(\mathbf{J})$, integrating over \mathbf{J} and summing over ℓ yields

$$\begin{aligned} & \sum_n a_n \left(\sum_{\ell_1} \int \psi_{\ell_1}^{(n)}(\mathbf{J}_1) f_{\ell_1}^{(p)*}(\mathbf{J}_1) d^2\mathbf{J}_1 \right) = \\ & \sum_{n'} a_{n'} \left(4\pi G \sum_{\ell_2, \ell_1} \int \int f_{\ell_1}^{(p)*}(\mathbf{J}_1) A_{\ell_1\ell_2}(\mathbf{J}_1, \mathbf{J}_2) \frac{m_2^{-1} \mathbf{m}_2 \cdot \partial F_0 / \partial \mathbf{J}_2}{\Omega_{\ell_2} - \Omega_p} \psi_{\ell_2}^{(n')}(\mathbf{J}_2) d^2\mathbf{J}_2 d^2\mathbf{J}_1 \right). \end{aligned} \quad (2.15)$$

Since $f_{\ell_1}^{(p)}$ belongs to the basis, it satisfies Eq. (2.13) and consequently

$$\sum_n a_n \left(\sum_{\ell_1} \int \psi_{\ell_1}^{(n)}(\mathbf{J}_1) f_{\ell_1}^{(p)*}(\mathbf{J}_1) d^2\mathbf{J}_1 \right) = \sum_{n'} a_{n'} \left(\sum_{\ell_2} \int \psi_{\ell_2}^{(p)*}(\mathbf{J}_2) \frac{m_2^{-1} \mathbf{m}_2 \cdot \partial F_0 / \partial \mathbf{J}_2}{\Omega_{\ell_2} - \Omega_p} \psi_{\ell_2}^{(n')}(\mathbf{J}_2) d^2\mathbf{J}_2 \right). \quad (2.16)$$

Requiring that Eq. (2.16) has non trivial solutions in $\{a_n\}$ leads to the dispersion relation

$$D(\omega) = \det |\mathbf{\Lambda} - \mathbf{M}(\omega)| = 0, \quad (2.17)$$

where the matrix \mathbf{M} is defined in terms of its components (n', p) by the bracket on the *r.h.s.* of Eq. (2.16) while the matrix $\mathbf{\Lambda}$ corresponds to the identity if the basis (ψ_n, f_n) is bi-orthonormal, or to a matrix with components components (n, p) by the bracket on the *l.h.s.* of Eq. (2.16) otherwise. Equations (2.17) was first derived in this context by Kalnajs (1977¹⁴). In order to approximate the behaviour of a halo, a supplementary parameter $q \in]0, 1]$ is introduced

$$D_q(\omega) = \det |\mathbf{\Lambda} - q\mathbf{M}(\omega)| = 0, \quad (2.18)$$

as discussed below.

2.3. Unstable modes & Nyquist diagrams

The dispersion relations (2.18) give, for each m , the criterion for the existence of exponentially growing unstable modes of the form $\exp(-i\omega t + im\theta)$. They are functions of a free complex parameter ω corresponding in its real part to m times the pattern speed of the growing mode, Ω_p , and in its imaginary part to the growth rate of the perturbation. The search for the growing modes is greatly facilitated by the use of Nyquist diagrams. Consider the complex ω plane and a contour that traverses along the real axis and then closes around the circle at ∞ with $\mathcal{I}m(\omega)$ positive. The determinant D_q is a continuous function of the complex variable ω , so as ω traces out the closed contour, $D_q(\omega)$ traces out a closed contour in the complex D_q plane. If the $D_q(\omega)$ contour encircles the origin, then there is a zero of the determinant inside the original contour and the system is unstable. In fact a simple argument of complex analysis shows that the number of loops around the origin corresponds to the number of poles above the line $\mathcal{I}m(\omega) \equiv \eta = \text{Constant}$. An intuitive picture of how the criterion operates on Eq. (2.17) is provided with the following thought experiment. Imagine turning up the strength of qG for the disk (*i.e.* turn on self-gravity, which is physically equivalent to allowing for the gravitational interaction to play its role; alternatively vary q , the ratio of relative halo support). Starting with small qG , all the M^{np} are small, so for all ω 's the determinant $D_q(\omega)$ remains on a small contour close to $\det |\mathbf{\Lambda}|$. As qG is increased to its full value, either the D_q contour passes through the origin to give a marginal instability or it does not. If it does not, then continuous change of qG does not modify the stability, and therefore the self-gravitating system has the same stability as in the zero qG case: it is stable. If, however, it crosses, and remains circling the origin then it has passed beyond the marginally stable case and is unstable. This picture is illustrated in the next sections where the image of the complex line $m\Omega_p + i\eta$, $\Omega_p \in]-\infty, \infty[$, is plotted for various values of η .

3. Numerical implementation

3.1. Method

Stability analysis, as implemented in the previous section, allows the treatment of a wide range of potentials and distribution functions which, in general, will not afford the explicit transformations between angle–action variables and velocity–position variables.

Spline interpolation for tabulated potentials and distribution functions is used to compute the transformation of variables by numerically integrating orbits in the given potential. The whole calculation is performed on a grid of points in (R_0, V_0) space where R_0 is the radius at apocentre, and V_0 the corresponding tangential velocity. As may be seen from figure Fig. 3.4 in the next section, a 40×40 grid is adequate for the disks considered here.

For each point in this grid, three orbits are calculated, one starting at the grid-point itself, and the others at small deviations in $h_0 = R_0 V_0$, and along $h_0 = \text{constant}$. The angles and actions for these orbits are used later to calculate numerical derivatives of the distribution function. A fourth order Runge-Kutta integration scheme is employed for the orbits, stopping at the first pericentre for all but the most eccentric orbits where more than one oscillation is needed to give sufficient accuracy in the actions. Further points on the orbits corresponding to grid vertices are then calculated at exact subintervals of the orbital period. The Fourier components ψ_ℓ^n of a particular basis element along an orbit Eq. (2.14) are then given by:

$$\psi_\ell^{(n)}(R_0, V_0) = \frac{1}{T_R} \int_0^{T_R} e^{-2\pi i \ell t / T_R} \psi^{(n)}(R[t]) e^{im\delta\theta(t)} dt, \quad (3.1)$$

where $t = \varphi_R / \kappa$ and

$$\delta\theta(\varphi_R) = \kappa^{-1} \int^{\varphi_R} \frac{h}{5R^2} d\varphi_R - \kappa^{-1} \frac{\varphi_R}{2\pi} \oint \frac{h}{R^2} d\varphi_R = \theta(t) - \langle \dot{\theta}(t) \rangle t. \quad (3.2)$$

Numerically, this simply corresponds to taking a discrete Fourier transform (DFT) over the re-sampled points. The symmetry of an orbit means that although the argument is complex, the result is purely real.

The matrix element defined in Eq. (2.16) is rewritten in terms of (R_0, V_0) and truncated in ℓ :

$$M^{(n)(n')}(\omega) = \sum_{\ell=-L}^{\ell=L} \iint \psi_\ell^{(n)*} \frac{(\partial F / \partial h \cdot m + \partial F / \partial J \cdot \ell)}{\Omega \cdot m + \kappa \cdot \ell - m\Omega_p - i\eta} \psi_\ell^{(n')} \left| \frac{\partial J \partial h}{\partial R_0 \partial V_0} \right| dR_0 dV_0 \quad (3.3)$$

where the $\psi_\ell^{(n')}$ are now surfaces in (R_0, V_0) space given by the ℓ 'th order term of the DFT of the orbit at R_0, V_0 .

The inclusion of retrograde stars may be effected transparently by specifying a grid in R_0, V_0 which includes negative V_0 or, more efficiently, by noting that

$$\psi_\ell^{(n)}(-h) = \frac{1}{\pi} \int_0^\pi \cos(\ell\varphi_R(-h) - m\delta\varphi(-h)) \psi^{(n)}(R[\varphi_R(-h)]) d\varphi_R, \quad (3.4a)$$

$$= \frac{1}{\pi} \int_0^\pi \cos(\ell\varphi_R(h) + m\delta\varphi(h)) \psi^{(n)}(R[\varphi_R(h)]) d\varphi_R, \quad (3.4b)$$

$$= \psi_{-\ell}^{(n)}(h), \quad (3.4c)$$

so with the appropriate sign switching the same set of orbits and Fourier modes may be used as for prograde stars.

Having calculated the derivatives of the distribution function with respect to J and h by finite differences across the slightly displaced orbits described earlier and the Jacobian $\partial(Jh)/\partial(R_0 V_0)$ in the same manner, the problem of computing the matrix elements of equation Eq. (3.3) reduces to one of integrating quotients of surfaces on the R_0, V_0 grid. It is worth noting that, although it is the steps of the calculation up to

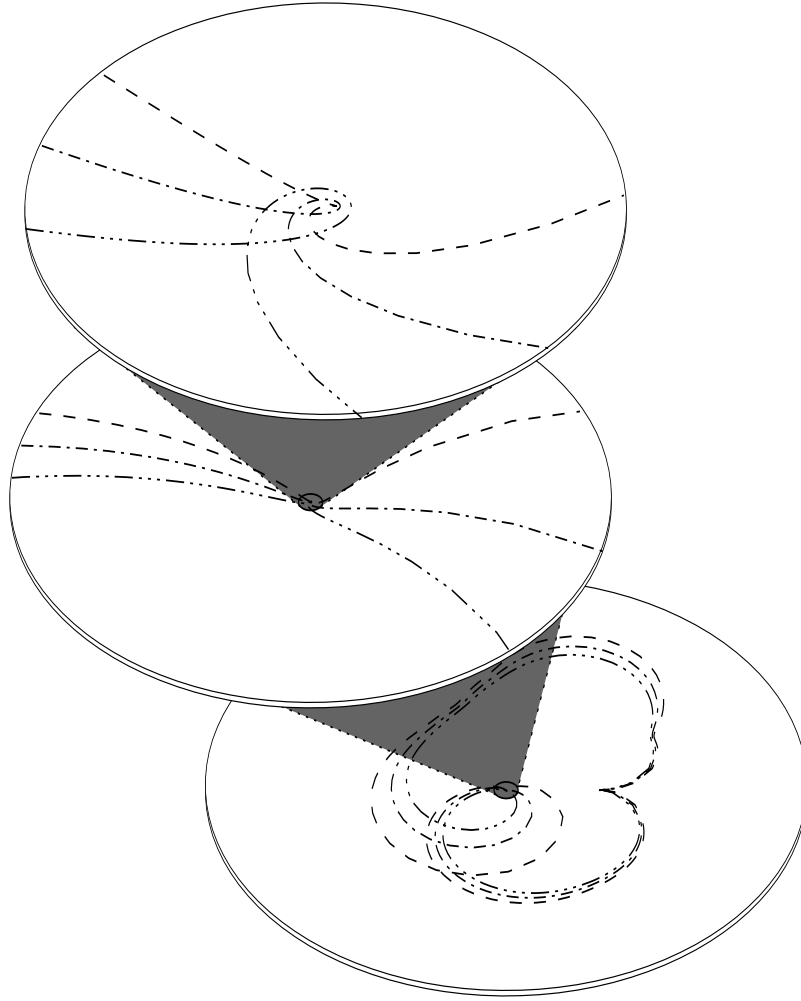


Figure 3.1: Nyquist diagram for the fastest growing mode of an isochrone/9 model for growth rates $\eta = 0.12$ (dashed curve), $\eta = 0.14$ (dot-dashed curve) and $\eta = 0.16$ (dot-long-dashed curve). The magnification shows that the first two curves do enclose the origin whereas the third does not, indicating that the true growth rate is between 0.14 and 0.16.

this point which provide the generality of the implementation, their computational cost is relatively slight amounting in total, for example, to about a minute on a workstation with a specFp92 of 100.

For vanishing growth-rates, the integrand in equation Eq. (3.3) is a quotient of surfaces with a real numerator but a denominator which may vanish along a line within the region of integration. The integral then exists only as a principal value integral. Rather than attempting a brute force discretisation we approximate both numerator and denominator by continuous piecewise flat surfaces and employ analytic formulae, or their power series expansions, for each flat subsection. Each square of the R_0, V_0 grid is treated as two triangles. According to the magnitudes and slopes of the two surfaces over a given triangle there are six different approximations to be used for each component of the integral. For modes with finite growth-rates, the integrand in equation Eq. (3.3) is of a quotient of surfaces with a real numerator but a complex denominator and this prescription still holds. The extra generality afforded yields a solution which handles transparently the marginal stability case, where the resonances can be infinitely sharp.

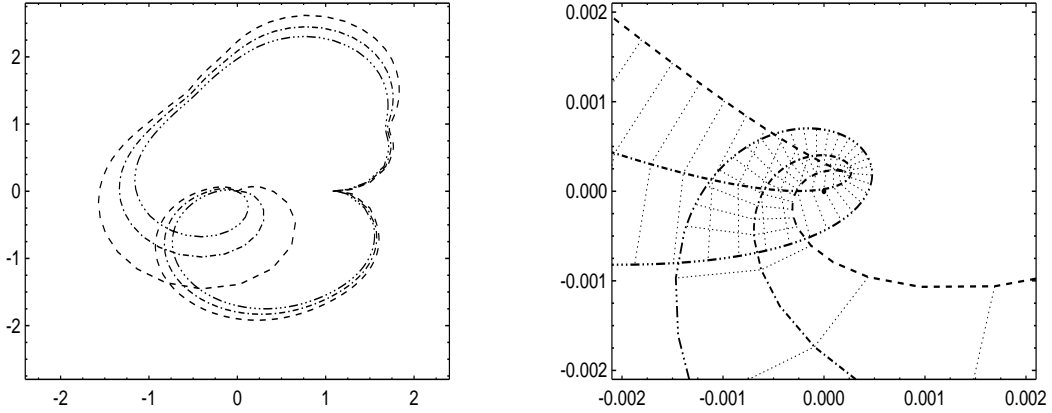


Figure 3.2: Nyquist diagram for the fastest growing mode of an isochrone/9 disk with curves labelled as on Fig. 3.1. The dotted lines join points of the same ω .

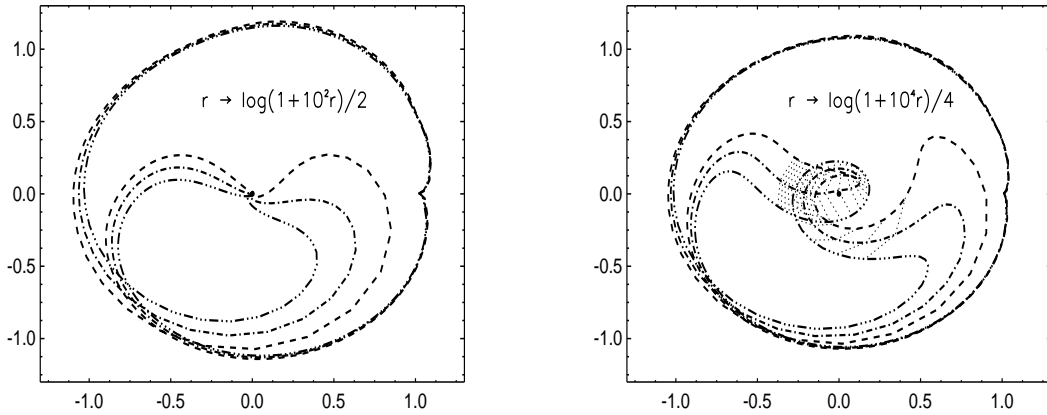


Figure 3.3: Nyquist diagram for the fastest growing mode of an isochrone/9 as in Fig. 3.1, Fig. 3.2. A logarithmic scaling has been applied near the origin mapping $r \rightarrow \log_{10}(1 + 10^\alpha r)/\alpha$ allowing the full topology to be seen more easily.

The integration and summation then yields, for each Ω_P and η , an $n \times n$ matrix M . Marginal stability corresponds to the vanishing of $\det|\mathbf{I} - \mathbf{M}|$. As described in section 2.3 it is convenient to use Nyquist diagrams to locate the critical points: matrices corresponding to a hundred or so values of ω are calculated for lines of constant η . Providing the sampling is good enough, the number of times the line $\det|\mathbf{I} - \mathbf{M}|$ encircles the origin in the complex plane gives the number of zeroes above the initial line $m\Omega_p + i\eta$. An example of Nyquist diagrams for the isochrone/9 disk (section 4) is illustrated in Fig. 3.1 and shown more quantitatively in Fig. 3.2 and Fig. 3.3. The 3-dots-dashed curve corresponds to $\eta = 0.16$ and does not encircle the origin, (or rather it loops once clockwise and once anticlockwise) whereas the other two curves ($\eta = 0.12$ and $\eta = 0.14$) do, indicating that the growth rate for the fastest growing bisymmetric instability of this disk is between 0.14 and 0.16.

This method is easy to apply to verify calculations where the growth rate and pattern speed are already known, but becomes more time-consuming when treating disks with unknown properties. Many automatic

schemes can be envisaged for locating zeroes in the complex plane but since computing the matrices is the slowest part of the calculation, we have found it most efficient to manage the search by hand with an interactive tool for examining Nyquist diagrams for different values of q (section 2.3). With a little experience the zeroes can be efficiently located even from poorly sampled diagrams with spurious loops which would easily lead to confusion in automated procedures.

3.2. Validation

There are two distinct types of errors to be assessed in this analysis: numerical errors arising from the discretization of integrals and from machine rounding; and truncation errors relating to the use of small finite bases, limited Fourier expansions and the calculation of only the inner parts of infinite disks.

While in principle constraining the first type of errors is purely routine, it is worth noting that both the bases considered here require the use of arbitrary precision languages (such as `bc`) for their evaluation. As noted by Earn & Sellwood (1995)⁷, Kalnajs' basis requires the use of about fifty figures precision to get the first thirty basis elements to five figures. The problem, however, lies only in evaluating the polynomial terms because the coefficients are large and induce substantial cancelations. Qian's basis (1992)²³ not only requires extended precision to evaluate a single element but it is also extremely close to being singular.

Besides evaluation of the basis elements, the only other part requiring special care is in the numerical derivatives of the distribution function with respect to J and h where a tight compromise must be made between the desire for a small interval to give an accurate derivative, and the loss of significance in the differences between angles and actions calculated for very close orbits. Nevertheless, a straightforward Runge-Kutta scheme for the orbits remains adequate in all the cases studied here.

The second class of errors – those arising from the truncation of equations Eq. (2.17) – are best assessed by simply recomputing the same quantity with more basis functions, more Fourier harmonics, or a larger disk. The results of these tests for all the truncated quantities can be seen in Fig. 3.4 and Fig. 3.5. All these results are for the isochrone/9 model first studied by Kalnajs (1976)¹³ with the $n = 7$ series of Kalnajs' basis functions, which is further discussed in the next section. Since the calculation of the matrix $\mathbf{M}(\omega)$ in Eq. (2.18) is the most computationally intensive operation, the self-gravity parameter q is taken instead of the growth rate η as a convergence criterion. The q plotted in the figures is that which satisfies Eq. (2.18). It is found by bisection with respect to the winding number of the Nyquist diagram. A value $q = 1$ for the expected exact growth rate (given by Kalnajs (1978)¹⁵) is the asymptote towards which the calculation should converge when the appropriate range of parameters have been found.

Fig. 3.4 shows how the sampling affects the result when the initial R_0, V_0 grid has the same number of points in each direction. The different lines in this and subsequent figures indicate how q converges for different sizes of basis. The figure shows that for this disk, a sampling with a 40×40 grid reduces the sampling errors well below those from the basis truncation. The right-hand figure shows how the truncation of the disk influences convergence for different sizes of basis. If the instability is localised to the inner parts of the disk, including more of the outer regions should not affect the result. The behaviour seen here is due to stretching of the basis when R_{\max} is increased, so more functions are required to sample the inner regions to the same resolution. If, however, enough functions are used, no change is seen beyond about $R_{\max} = 4.5$.

As remarked by Earn and Sellwood (1995)⁷ choosing an appropriate basis for a given instability has a significant effect on the number of basis functions necessary to resolve the mode. This may be seen in Fig. 3.5 for Kalnajs' set of biorthonormal bases with $4 \leq k \leq 10$. Ten functions with the $k = 4$ basis are required to give the same error in q as achieved with only six functions in the $k = 10$ basis. Kalnajs' remarks that some economies may be made by not using the same number of positive and negative radial Fourier modes but by centering the range on m , the order of the instability. This is illustrated in the right-hand figure, where the abscissa gives the number of radial modes on each side of a central value as labelled. The computational load is almost directly proportional to the number of radial modes to be used so this effect is well worth exploiting. Developing specific basis for different thin disks also speeds up the calculation, by reducing the number of functions required for convergence but it is not necessary. Any reasonable basis will get there in the end and the feasibility of the resulting computations considerably enhances the generality of this approach.

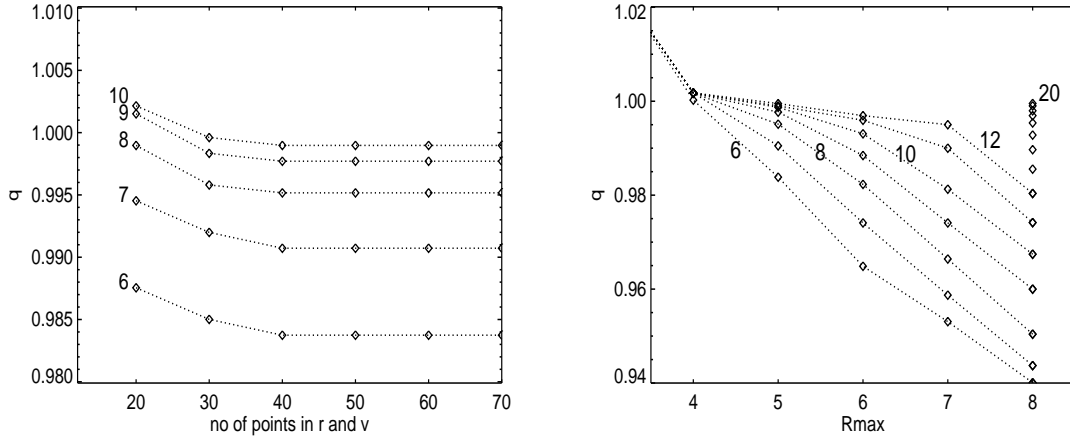


Figure 3.4: The self-gravity parameter, q as a function of the grid sampling, and the disk truncation. Data are shown for bases of various sizes as labelled. On the right, q is shown as a function of the truncation radius of the disk for different sizes of basis as labelled. More functions are needed for convergence with larger R because the inner, dominant, part of the disk is less well sampled when the basis is stretched over a larger domain. As with all the figures in this section, the disk is Kalnajs' isochrone/9 model. The basis is Kalnajs' biorthonormal set with $k = 7$.

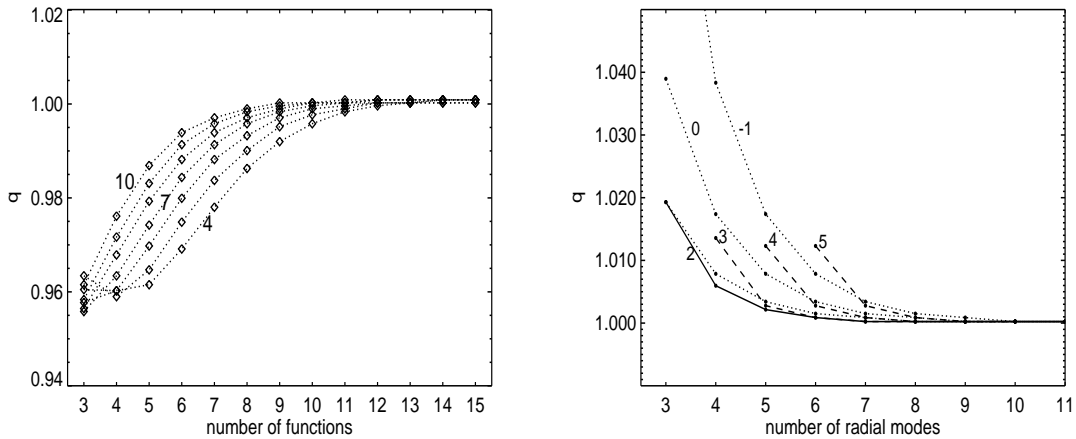


Figure 3.5: The dependence of the self-gravity parameter, q , upon the order of the basis, the number of functions used in the calculation, and the number of radial harmonics. The left-hand figure shows q against the basis size for different bases from Kalnajs' set, labelled by the corresponding k parameter. On the right, 12 functions were used, with the number of radial harmonics on the abscissa taken on either side of a central value as labelled on the lines. Centering the harmonics on 2 (when looking for bi-symmetric instabilities) shows appreciably better convergence than taking equal numbers of positive and negative harmonics (centre 0).

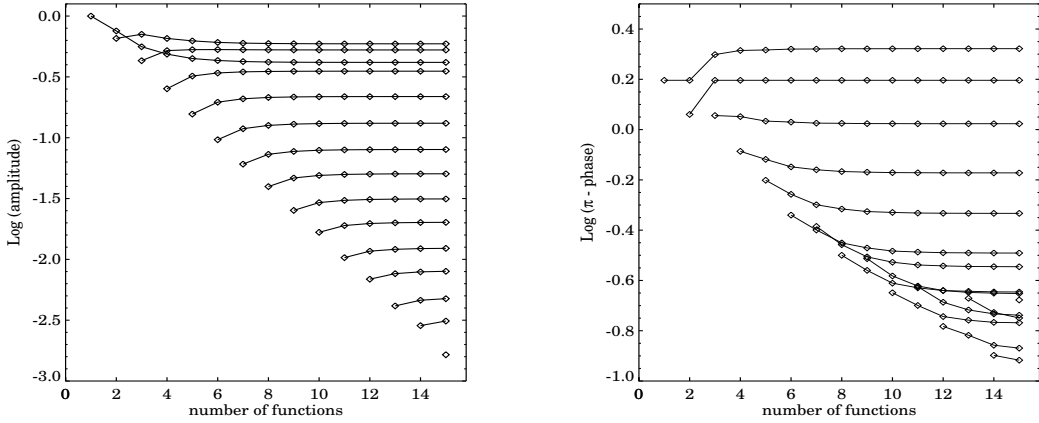


Figure 3.6: The amplitude (left panel) and the phase (right panel) of components of the critical eigenvectors as a function of the number of basis functions. The rapid convergence of the shape of the mode appears clearly.

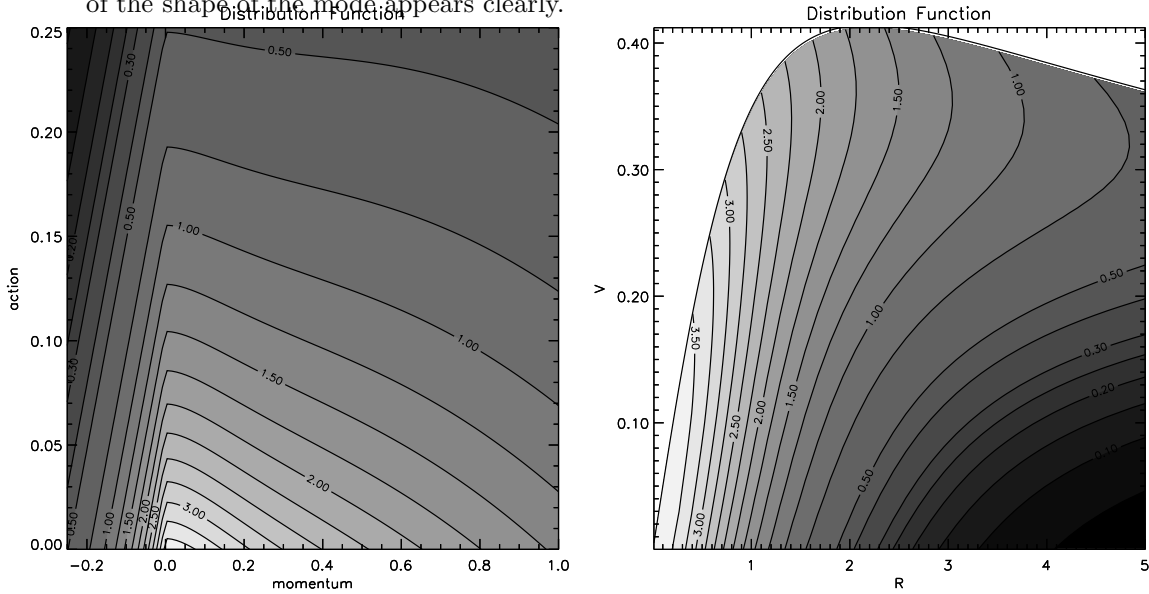


Figure 4.1: left panel: isocontours of the $m_P = 4$ distribution function in action space. The sharp break at zero momentum is an artifact of Kalnajs's trick which was used here to incorporate counter rotating stars; right panel: same isocontours for the prograde stars only in (R_0, V_0) – apocentre, velocity at apocentre – space. These variables are those used throughout the calculation to label the orbits. Note the envelope corresponding to the rotation curve of that galaxy. It appears clearly in this parametrisation that in this galaxy most orbits are of low ellipticity.

4. Application: The isochrone and Kuzmin-Toomre disks

The versatility of the algorithm for linear stability described above is now illustrated while recovering growth rates and pattern speeds of previously studied disk with old and new distribution functions, finding the modal response – in position space and in action space – of these disks both for bi-symmetric and lopsided modes.

Table 4.1: $m = 2$ growth rates and pattern speed of the isochrone/ m_K model.

The isochrone/ m_K model: bi-symmetric mode		
Model	$m\Omega_p$	η
6	0.34	0.075
7	0.37	0.085
8	0.43	0.125
9	0.47	0.145
10	0.50	0.170
11	0.53	0.195
12	0.59	0.210

4.1. The Equilibria

Three families of disks are studied here: two corresponding to equilibria for the isochrone disk (1961)¹⁰, and one for the Kuzmin-Toomre (1956)¹⁶ mass model. The isochrone disk is defined by its potential, $\psi = GM/(b + r_b)$ where $r_b^2 = R^2 + b^2$. The corresponding surface density is $\Sigma = Mb \{ \ln[(R + r_b)/b] - R/r_b \} / (2\pi R^3)$. The Kuzmin-Toomre potential is defined by $\psi = GM/r_b$ and the corresponding surface density is $\Sigma = Mb/2\pi r_b^3$. Miyamoto (1974)¹⁹, followed by Kalnajs (1976)¹³, Athanasoula & Sellwood (1985)¹, and Pichon & Lynden Bell (1996)²¹ chose specific forms of distribution functions assuming simple algebraic Ansatz for its expression in (ε, h) space. Historically, these models were first used to construct families of maximally rotating disks (*e.g.* the Miyamoto/ m_M disk models¹¹) while for others, counter-rotating stars were re-introduced by simple, though somewhat arbitrary, tricks (Kalnajs (1978)¹⁵ described by Earn & Sellwood(1995)⁷). In this paper, The Kalnajs isochrone/ m_K models are implemented in order to recover Kalnajs (1978)¹⁵ first linear stability results on differentially rotating disks. To demonstrate the flexibility of the method the truncated version of Hunter's Toomre-Kuzmin/ m_M models are also constructed, and the stability of the equilibria given by Pichon & Lynden Bell (1996) are analysed.

Kalnajs's distribution family reads (in units of b and $G = 1$)

$$f_K(\varepsilon, h) = 2^{2m-1} (\sqrt{-2\varepsilon h})^{-m} \pi^{-1} (-\varepsilon)^{m-1} g(\sqrt{-2\varepsilon h}), \quad (4.1)$$

where

$$g(x) = x \frac{\partial (x^m \tau_m(x))}{\partial x} + \int_0^1 (tx)^m \tau_m(tx) P''_{m-1}(t) dt - \frac{1}{2}(m-1)mx^m \tau_m(x), \quad (4.2)$$

and

$$\tau_m(x) = \frac{\log(r + \sqrt{1+r^2}) - r/\sqrt{1+r^2}}{2\pi r^3 (-1 - \sqrt{1+r^2})^{-m}} \Bigg|_{r=2x/(x^2-1)}. \quad (4.3)$$

Here P_m stands here for the Legendre polynomial of order m . Pichon and Lynden-Bell's distribution family for the isochrone disk is given by

$$f_P(\varepsilon, h) = \frac{(-\varepsilon)^{m+1/2}}{4\pi^2 (m+1/2)!!} \frac{h}{\sqrt{2}} \left(\frac{\partial}{\partial s} \right)^{m+2} \left[(s^2 - 1)^m L(s) \right] \Bigg|_{s=1+h^2/2}, \quad (4.4)$$

with $L(s) = \log(\sqrt{s^2 - 1} + s) + \sqrt{s^2 - 1}/s$. Its contours for $m_P = 4$ are illustrated in Fig. 4.1 while the Q profiles are given by Pichon & Lynden Bell (1996)²¹ (Fig PLB 5). Finally Miyamoto's distribution is

$$f_M(\varepsilon, h) = \frac{(2m+3)}{2\pi^2} (-\varepsilon)^{2+2m} {}_2F_1 \left(-m, -2-2m, \frac{1}{2}, \frac{-h^2}{2\varepsilon} \right), \quad (4.5)$$

where ${}_2F_1$ is a terminating Hypergeometric function of the second kind.

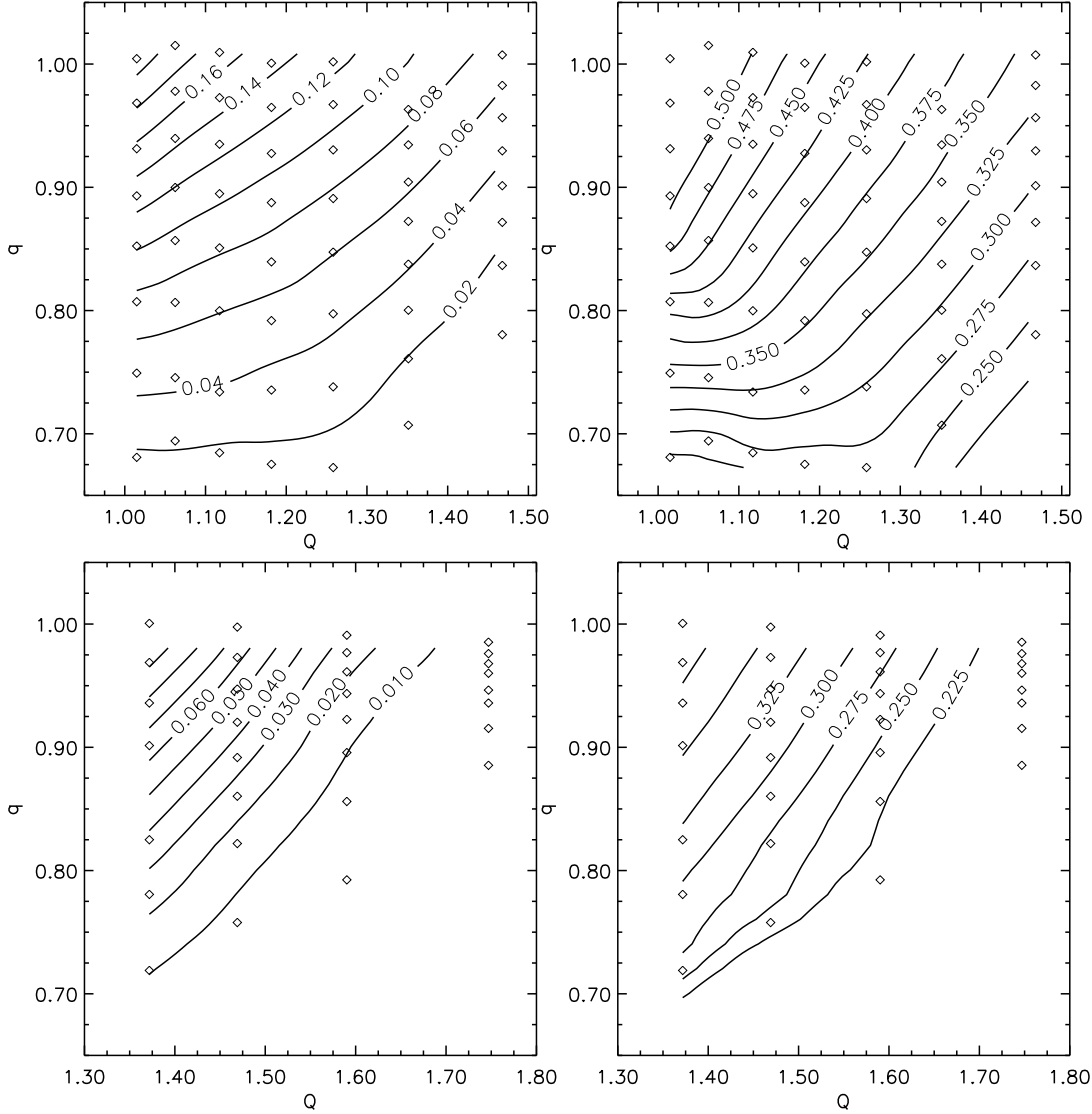


Figure 4.2: the variation of the $m = 2$ growth rate (top left panel) and the pattern speed (top right panel) of an isochrone/ m_K family as a function of the self gravity parameter q and the Toomre number Q . The bottom panels show the same results for the isochrone/ m_P family. The precision in the growth rates – at fixed truncation in the basis – drops for lower values of Q since these modes are more centrally concentrated.

4.2. Characteristics of the linear wave

4.2.1. Bi-symmetric $m = 2$ modes

The pitch angle of the spiral response is commonly defined as $\cot(i) = \langle \partial\theta / \partial \log(R) \rangle_\theta$ where $\theta = \theta(R)$ at the crest of the spiral wave. In practice, it is best to calculate $\tan(i) = \langle \partial \log(R) / \partial \theta \rangle_R$ since $R = R(\theta)$ is a bijection in $[0, 2\pi/m[$. Another useful set of quantities are defined by the radius, $R_{1/2}$, (resp. the angle $\theta_{1/2}$) at which the spiral response has decreased to half its maximum amplitude. The winding number $n_{1/2} = \theta_{1/2} / (2\pi)$ yields a measure of the winding of the wave: the larger $n_{1/2}$ the more wound it is. Comparing the position of the resonances and R_{\max} to $R_{1/2}$ provides means to assess whether the truncation of the disk is likely to have generated spurious cavity waves. Specifically, it is required that $R_{1/2} < R_{\text{OLR}} < R_{\max}$ so that the wave is well damped by the outer Lindblad resonance before the disk is truncated. Numerical simulation have suggested that $R_{1/2} \sim R_{\text{COR}}$. Both statements are verified here for instance in Fig. 4.4 (resp. Fig. 4.5) which

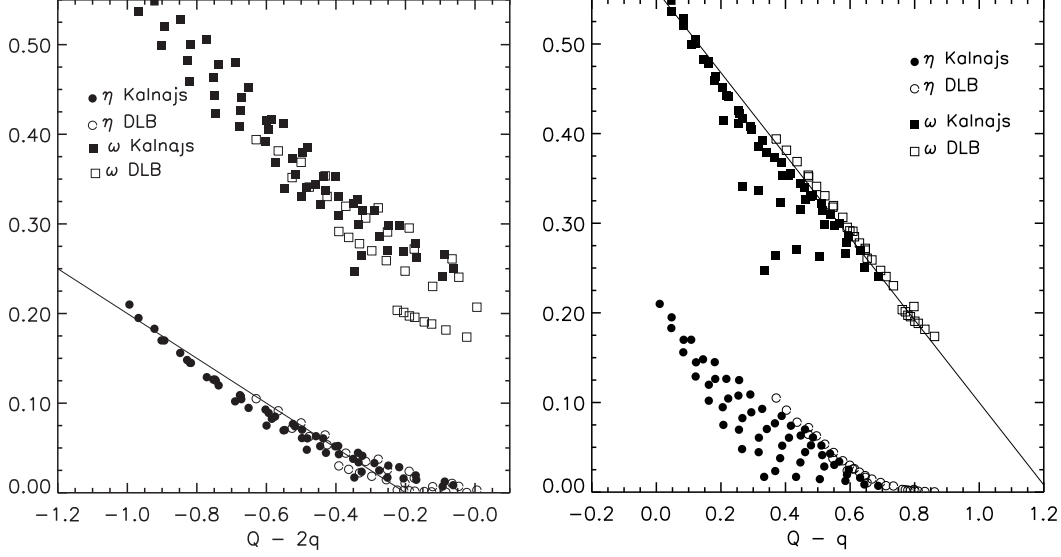


Figure 4.3: fits to the evolution of the $m = 2$ growth rate and the pattern speed of an isochrone/ m_K (marked Kalnajs) and an isochrone/ m_P (marked DLB) family as a function of a linear combination of the self gravity parameter q and the Toomre number Q . The left panel minimises the dispersion in η whereas the right panel that in ω . The best fits are obtained for different linear combinations of Q and q . The solid line for η is $\eta = -0.05 - 0.25(Q - 2q)$ and that for ω : $\omega = 0.56 - 0.46(Q - q)$.

Table 4.2: $m = 2$ growth rates and pattern speed of the isochrone/ m_P model.

The isochrone/ m_P model: bi-symmetric mode		
Model	$m\Omega_p$	η
3	0.21	0.003
4	0.29	0.032
5	0.35	0.072
6	0.40	0.105

Table 4.3: $m = 2$ growth rates and pattern speed of the Toomre/ m_M model.

The Toomre/ m_M model: bi-symmetric mode		
Model	$m\Omega_p$	η
2	0.598	0.204
3	0.714	0.294
4	0.810	0.371
5	0.916	0.445

gives the linear response of a $m_K = 7$ and a $m_K = 11$ isochrone disk (resp. $m_K = 5$ Kuzmin disk) for its first growing mode. These perturbations display the usual bar shaped central response with a loosely wound spiral response further out. Fig. 4.6 gives the evolution of $\cot(i)$, $R_{1/2}$, $n_{1/2}$, Ω_p , η , as a function of the Toomre number Q of the Kalnajs $/m_K$ disks. Table 4.1-Table 4.3 give the growth rates and pattern speeds of the $/m_K /m_P$ and $/m_M$ families. Note that for the new $/m_P$ family the bar mode given in Table 4.2 again have pattern speed well above the maximum of $\Omega - \kappa/2$ and hence do not display inner Lindblad resonance. Note also that the more compact Kuz'min -Toomre potential has larger growth rates and pattern speed as

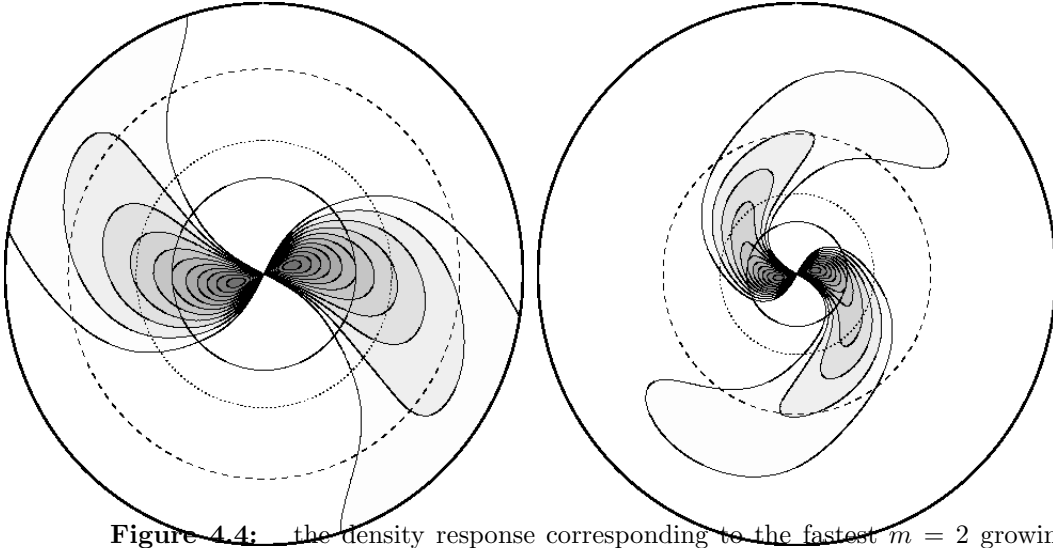


Figure 4.4: the density response corresponding to the fastest $m = 2$ growing mode of the isochrone/7 and isochrone/11 model. Note that the colder /11 model yields a more tightly wound spiral as shown quantitatively in Fig. 4.6. This is expected since in the locally marginally radially unstable régime, the disk response should asymptotically match that of unstable rings. Its spiral response is also more centrally concentrated than that of its hotter counterpart. The solid circle corresponds to $R_{1/2}$, the radius at which the wave has damped by a factor of two; the dotted circle to Corotation resonance; the dashed circle to the outer Lindblad resonance and the outer circle to $R_{max} = 5$.

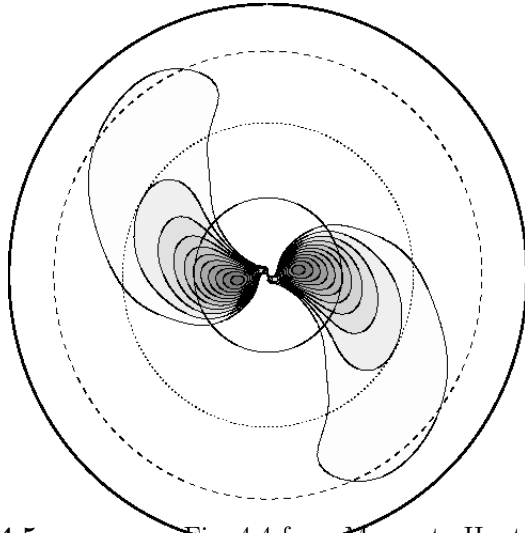


Figure 4.5: same as Fig. 4.4 for a Myamoto-Hunter/3 model. Note that the response is much more centrally concentrated since the outer circle is $R_{max} = 3$. This is expected since the Kuzmin-Toomre potential is more compact than the isochrone.

expected since the dynamical time is shorter and the self gravity enhanced for those disks. Table 4.4 gives the growth rates for the second and the third growth rate of the m_K disks. Note that the growth rate of the second fastest growing mode of a $m_K = 12$ model was found by this method to equal $\omega + i\eta = 0.461 + 0.145i$, roughly within the error bars given by Earn & Sellwood (1995)⁷. Note that the number of radial nodes for these slower modes increase with the rank in stability (as illustrated in Fig. 4.10 for a $m = 1$ mode discussed in the next subsection) which is consistent insofar as winding decreases self gravity. Note also the

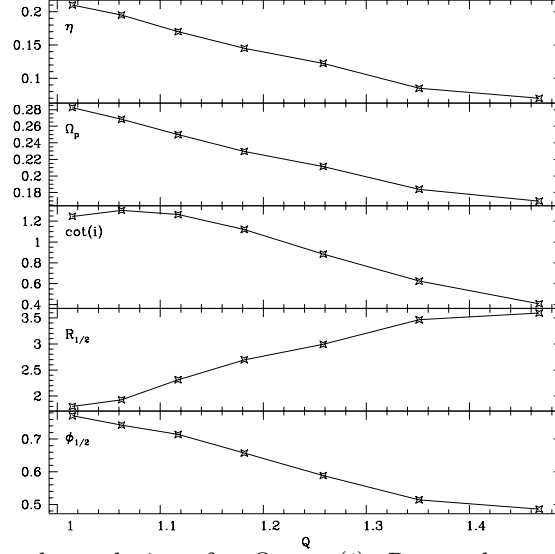


Figure 4.6: the evolution of η , Ω_p , $\cot(i)$, $R_{1/2}$ and $n_{1/2}$, as a function of the Toomre number Q of the isochrone/ m_K disks. Note that the hotter disk have less wound spiral response.

Table 4.4: second and third fastest $m = 2$ growing modes of the isochrone/ m_K model.

The isochrone/ m_K model: bi-symmetric mode		
Model	second mode	third mode
7	$0.29(4) + 0.04(1)i$	$0.22(0) + 0.008(8)i$
10	$0.39(7) + 0.10(5)i$	$0.27(3) + 0.039(5)i$
11	$0.42(8) + 0.12(8)i$	$0.34(7) + 0.091(5)i$
12	$0.46(1) + 0.14(5)i$	$0.26(4) + 0.051(2)i$

small relative error between the growth rates recovered for the Myamoto/Hunter models and those given by Hunter (1993)¹¹ for the Toomre-Kuzmin disks. Small residual discrepancies are expected given that Hunter's disks are infinite whereas those studied here are truncated at $R = 5$. Fig. 4.2 gives for the m_K and m_P families the evolution of the first growing mode as a function of the Toomre Q number (mass averaged in the inner region $R < 2$) of these disks and “the mass in the halo” as parametrised by q . A new attempted fit of a combination of Q and q is also given in Fig. 4.3 for both distributions; the relative dispersion illustrates the well known fact that the stability does not depend only on a simple combination of these numbers. These curves seem to be in qualitative agreement with those given by Vauterin & Dejonghe²⁶ for different disk models. Here too, the pattern speed at fixed growth rate is a decreasing function of the Q number ($\partial\Omega_p/\partial Q_\eta < 0$). The conjecture of Athanasoula & Sellwood¹ of an asymptotic value of $Q \approx 2$ for marginal stability of *fully self gravitating* disk seems also consistent with these results.

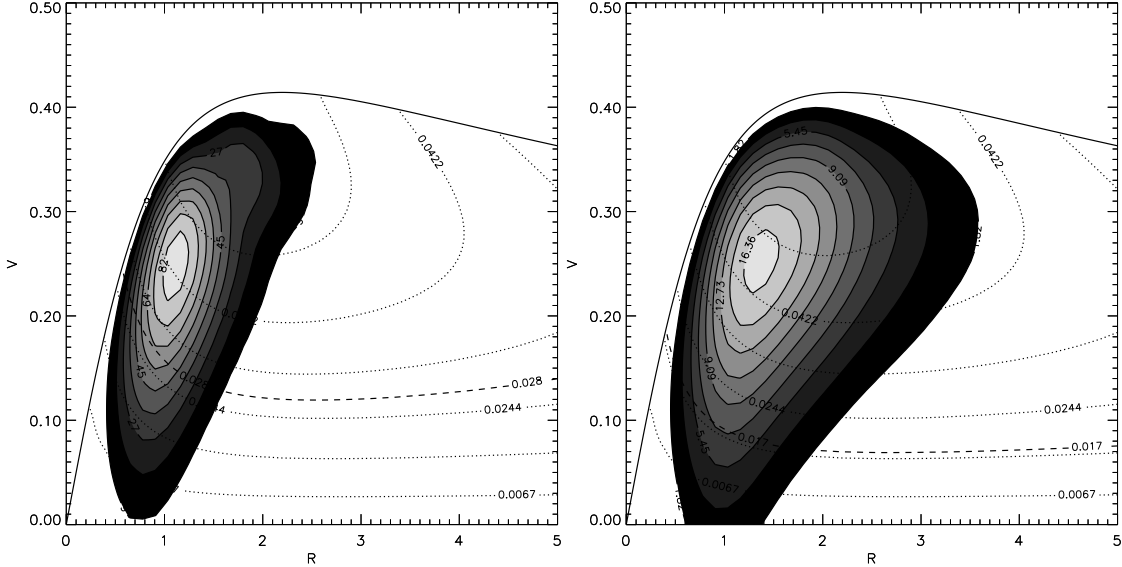


Figure 4.7: the orbital response in action space corresponding to the fastest growing mode described in Fig. 4.4. The amplitude of the left hand side of Eq. (2.5) is plotted for the $\ell = -1$ (ILR) fastest growing mode of an isochrone/12 model (left panel), and an isochrone/6 model. (right panel). Superimposed are the isocontours of the corresponding resonance $\Omega - \kappa/2$. The dashed line corresponds to the isocontour of a tenth of the pattern of the wave. Note that the hotter disk forms a Grand Design structure involving more eccentric orbits.

4.2.2. Lopsided $m = 1$ modes

The algorithm presented in section 3 is in principle inadequate to address the growth of $m = 1$ perturbations which for purely self gravitating disks are forbidden since the perturbation does not conserve momentum. Following Zang²⁷, it is assumed here that the disk is embedded in some sufficiently massive halo to compensate its infinitesimal centre of mass shift. Fig. 4.9 gives the $m = 1$ modal response of the isochrone/ $m_{10,11}$ disks while the corresponding pattern speeds and growth rates are given in Table 4.5. These modes have smaller growth rates than their bi-symmetric counterparts and are practically more difficult to isolate because they are close to other modes which grow almost as fast; the nyquist diagrams show many large loops, all of which must be properly sampled to avoid spurious contours encircling the origin as illustrated in Fig. 4.8. Indeed, when investigating weaker and weaker modes the amount of looping in the corresponding nyquist diagrams should increase since modes always occur in pairs ($\omega \pm \eta$) so that when η is small one is always in a régime corresponding at least to two (a growing and a decaying) modes.

The physical mechanism leading to the appearance of these modes needs to be clarified, but presents little practical interest when their growth rates do not correspond to the fastest growing mode. The detailed analysis of $m = 1$ modes for the isochrone disk is therefore delayed until models of distribution functions which display weaker $m = 2$ modes are designed.

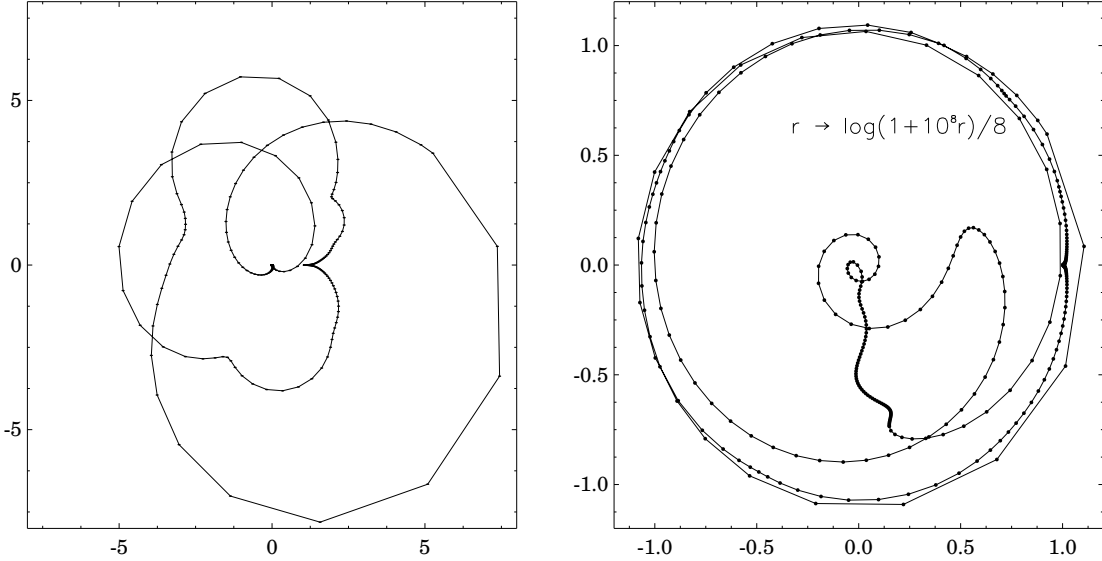


Figure 4.8: Nyquist diagram for the second $m = 1$ modes of the an isochrone/12 disk. There are more large loops than are seen for the bi-symmetric modes, and also more structure at small scales: on the right, the origin is shown enlarged under the mapping $r \rightarrow (1 + 10^8 r)/8$. All the space within the innermost of the three large concentric loops corresponds to the tiny cusp at the centre of the left hand panel.

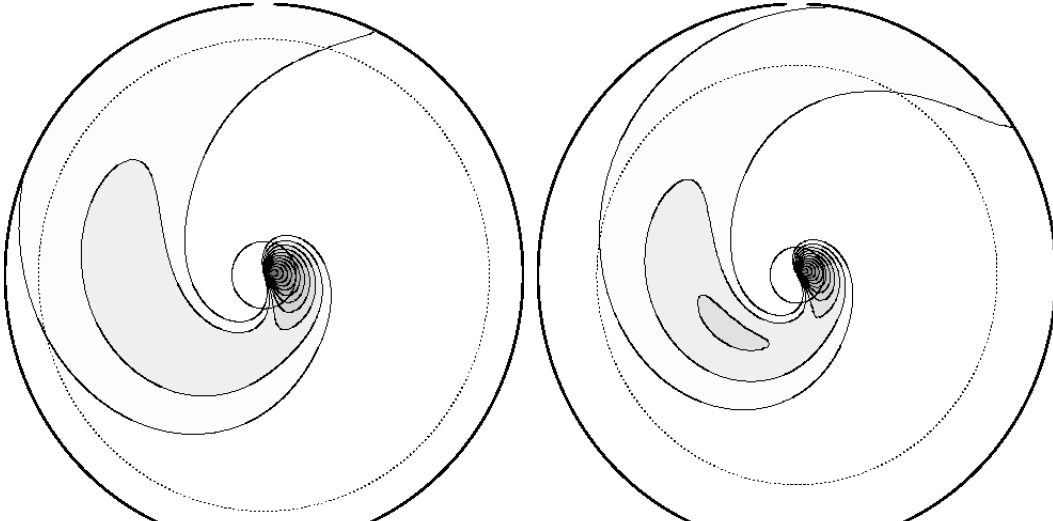


Figure 4.9: the $m = 1$ density response corresponding to the growing mode of the isochrone/10 and isochrone/11 model. The lopsided mode, which has a smaller growth rate, has a much more centrally concentrated response than its bi-symmetric counterpart.

4.3. Application to observed disks

The procedure described in section 3 makes no assumption on the nature of the distribution function or the potential of the disk. In particular, it is well adapted to distribution functions recovered from measured disks, where the radial derivative of the potential follows from the HI rotation curve of the disk while the distribution function itself is inverted from line of sight velocity profiles. The technique was tested on tables generated from Eq. (4.5). The agreement between the “theoretical” and “measured” (*i.e.* derived from a discretized representation of the distribution) growth rates was found to be in better than one percent. One peculiarity in this context lies in the finite difference chosen in the numerical derivatives of the distribution

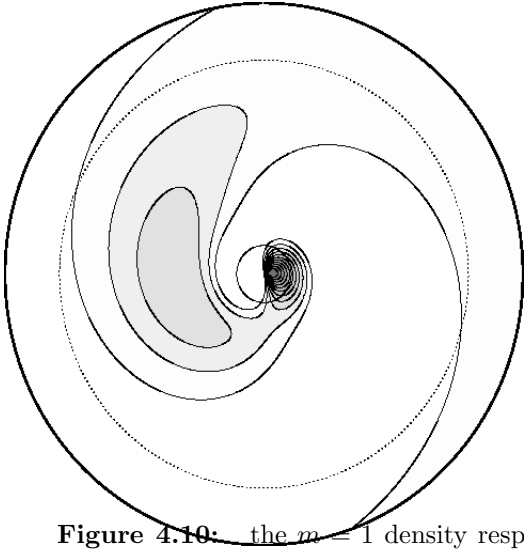


Figure 4.10: the $m = 1$ density response corresponding to the second faster growing mode ($\Omega_p + i\eta = 0.18 + i 0.075$) of the isochrone/12 model. The number of radial nodes in the response has increased by one compared to the corresponding faster mode illustrated on Fig. 4.9 for an isochrone/11 disk.

Table 4.5: first and second growth rates and pattern speed of the $m = 1$ isochrone/ m_K model.

The isochrone/ m_K model: lopsided mode		
Model	pattern speed	growth rate
9	0.135	0.0325
10	0.17	0.065
11	0.20	0.095
12	0.23	0.125

function with respect to J and h . While applying this analysis to observed data, special care should be taken in handling measurements relative to the core of the galaxy, since the relative fraction of counter rotating stars plays a crucial role in determining the growth rates of the disk, as pointed out already by Kalnajs and illustrated in Fig. 4.11. This appears clearly when recalling that counter-rotating stars add up to an effective azimuthal pressure in the inner core which therefore prevents the self gravity of the disk to build up by orbit alignment. A non parametric inversion technique has been devised by Pichon & Thiébaud (1997)²² to recover the best distribution accounting for all the measured kinematics while handling specifically the counter-rotating stars.

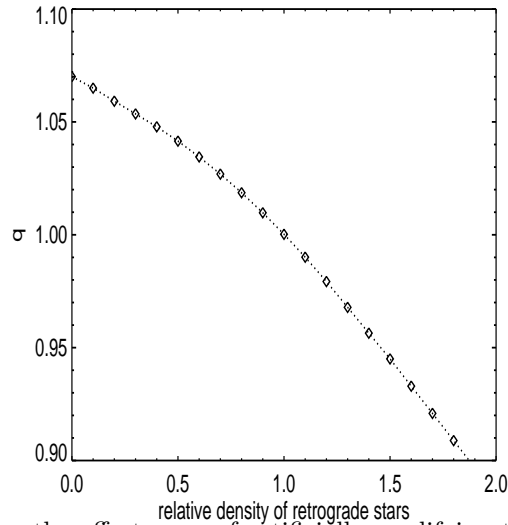


Figure 4.11: the effect on q of artificially modifying the density of retrograde stars in Kalnajs’ isochrone/9 distribution function. The retrograde part of the distribution function has been multiplied by the factor on the ordinate, keeping the prograde stars the same. Although in Kalnajs’ model stars on retrograde orbits only account for a few percent of the total mass, they play a significant role in stabilising the disk.

5. Conclusion & prospects

A numerical investigation of linear stability of round galactic disks has proven successful in recovering known growth rates for the isochrone disk and the Kuzmin Toomre disks. The method is fast and versatile, and can be applied to realistic disks with arbitrary density and velocity profiles and relative “halo” support. Unstable bi-symmetric growing modes for *new* equilibria, and the fastest growing lopsided modes for Kalnajs’ distribution function have also been isolated to demonstrate the code’s versatility. The authors are currently applying the method in a study of the stability to families of disks parametrised by their relative temperature, compactness, fraction of counterrotating stars and halo support in order to identify the orbits responsible for the instability, and to probe the intrinsic (orbital or wave-like) nature of the $m = 2$ bar instability. The nature of lopsided $m = 1$ instabilities in disk galaxies is also under investigation. The implementation of linear stability analysis for observed galactic disk, yielding a direct relationship between the growth rate of the instability, the measured kinematical characteristics of the disk and the relative mass in the halo is also being investigated. The requirement of marginal stability will provide an estimate of the minimum halo mass. All ingredients will then be in place to probe the amount of dark matter required to stabilise observed galactic disks.

Acknowledgements

CP wishes to thank J. Collett, D. Lynden-Bell, S. Tremaine, J.F. Sygnet and O. Gerhard for useful conversations. Many thanks to the referee, J. Sellwood, for positive criticism, to J. Binney for reading the manuscript and to P. Englemaier for his help with sm. Funding from the Swiss NF and computer resources from the IAP are gratefully acknowledged.

References

1. Athanasoula, E. and Sellwood, J. “*Bi-symmetric instabilities of Kuzmin-Toomre disks.*” MNRAS 221, 213-232 (1985).
2. R. Bender, R. Saglia, & O Gerhard., MNRAS 269, 785-813 (1994).
3. Bertin, G., “*Linear stability of spherical collisionless stellar systems*” ApJ 434, 94B (1994).
4. Collett, J., (1995) “*Isocirculational mechanics in stellar systems*” PhD, Cambridge.
5. Lynden-Bell, D. and Kalnajs, A. “*On the generating mechanism of spiral structures.*” MNRAS 157, 1-30 (1972).
6. Clutton-Brok, M MNRAS 157, 1-30 (1972).
7. Earn, D. and Sellwood, J. “*The optimal N-body method for stability studies of galaxies.*” Astrophysical Journal v.451, p.533 , 0-0 (1995).
8. Earn, D., (1993) PhD, Cambridge.
9. Hohl F. ApJ 168, 343 (1971).
10. Henon, M. “.” Ann. d’Astrophys, 23 668 (1960)..
11. Hunter, C. “*Instabilities of stellar discs.*” Astrophysical disks ed. S.F. Dermott. J.H. Hunter and R.E. Wilson (New York New York Accademy of Sciences (1993).
12. Kalnajs, A. “*Dynamics of Flat Galaxies. I.*” ApJ 166, 275-293 (1971).
13. Kalnajs, A. “*Dynamics of Flat Galaxies II, Biorthonormal Surface density potential pairs for finite disks.*” ApJ 205, 745-761 (1976).
14. Kalnajs, A. “*Dynamics of Flat Galaxies VI, The Integral Equation For Normal Modes in Matrix Form.*” ApJ 212, 637-644 (1977).
15. Kalnajs, A.(1978) in Berkhuisjen, E. Wielebinski, R. eds. Proc. IAU Symp. **77**, “Structures and properties of nearby galaxies.” p. 113.
16. Kuzmin, G. G. Astr. Zh. 33 27 (1956).
17. Lynden-Bell, D. and J. Ostriker “*On the Stability of Differentially Rotating Bodies.*” MNRAS 136, 293-310 (1967).
18. Lynden-Bell, D. “*On a Mechanism that Structures Galaxies.*” MNRAS 187, 101-107 (1979).
19. Miyamoto “*A class of disk-like models for self-gravitating stellar systems*” Astronomy & Astrophysics 30, 441-454 (1974).
20. Pichon, C. and Lynden-Bell, D. “*Orbital instabilities in galaxies*”, contribution to the “Ecole de Physique des Houches” on: Transport phenomena in Astrophysics, Plasma Physics, and Nuclear Physics.
21. Pichon, C. and Lynden-Bell, D. “*The equilibria of flat and round disks*”, MNRAS. (1996) **282** (4), 1143-1158..
22. Pichon, C. and Thiébaud, E. “Distribution functions for observed galactic disks: a non parametric inversion”, submitted to MNRAS (1997).
23. Qian, E. “*Potential-Density Pairs for Flats Discs.*” Monthly Notices of the Royal Astronomical Society 257, 581-592 (1992).
24. Sellwood, J. and A. Wilkinson “*Dynamics of barred galaxies.*” Rep Prog Phys 56, 173-255 (1993).
25. Sygnet, J.F. & Kandrup “A simple proof of dynamical stability for a class of spherical clusters” ApJ 276, 737 (1984).
26. Vauterin,P. & Dejonghe,H. , AA 313, 465-477 (1996).
27. Zang, T., (1976) “*The stability of a Model Galaxy*” PhD thesis, MIT.
28. Weinberg, M. D., ApJ 368, 66 (1991) .